Semi-globally Asymptotically Stable Nonlinear Observer for Camera Aided Navigation

Elias Bjørne* Edmund Førland Brekke* Torleiv Håland Bryne* Tor Arne Johansen*

***Abstract*— This article presents a nonlinear observer that performs range estimation as well as gyro bias estimation by using velocity, angular rate and bearing angle measurements from landmarks at unknown locations. The observer is proved to have semi-global asymptotic stability, and its performance is verified in simulations and on experimental data. The observer is demonstrated on an unmanned aerial vehicle (UAV) with a sensor setup consisting of camera, inertial measurement unit (IMU), and velocity measured by a global navigation satellite system (GNSS). This sensor suite is sufficient to replace the magnetometer and the altimeter.**

***Index Terms*— Attitude observer, Navigation, Nonlinear Observer, Sensor data fusion, Localization**

I. INTRODUCTION

Camera-aided inertial navigation has been extensively studied. Some setups rely on having landmarks with known position, which is refereed to as the perspective n point (PnP) problem [1], while bearing-only simultaneous localization and mapping (BO-SLAM, also called mono- and visual-SLAM) estimates the *unknown* positions of the landmarks. Many of the solutions are based on either some form of extended Kalman filter (EKF) [2], [3], [4] or a nonlinear optimization scheme [5], [6]. This has proven to give accurate results, although robustness and computational load remain to be challenging. Hence there has recently been an increasing effort to investigate solutions to these problems with global convergence guarantees [7], [8], [9], [10], [11], [12]. It should, however, be stated that all these methods depends on having a velocity measurements and either having a calibrated IMU without gyro bias, or an attitude heading reference system (AHRS) available. In [8], [9] they also demonstrate how such an observer could be expanded to estimate bias in the velocity measurements. However, these observers are unable to estimate and compensate for any gyro bias.

In this article we present a novel observer, where we have expanded the observer in [12] to also handle gyro bias estimation. It filters the velocity and bearing measurements from landmarks, in order to estimate the ranges to the landmarks as well as gyro bias. It can also be used for bearing-only SLAM if it is combined with a loop-closing front-end system [13]. It will be presented with a proof of semi-global asymptotic stability and exponential stability in the large. The observer is demonstrated in simulations, where a sensor setup with a camera, GNSS and IMU for a UAV is used. The observer is able to provide range/altitude estimates as well as estimating the gyro bias. The observer is validated experimentally, and the gyro bias observer is used in a cascade with an attitude estimator [14]. The attitude observer is also compared to a simpler velocity-aided attitude observer based on a nonlinear complementary filter [15].

The structure of this paper is as follows: Notation and preliminaries are presented in Section II; Section III presents the novel estimator and proof of its stability properties; while Section IV shows simulation results. In Section V the results of the experimental validation are presented and finally, Section VI concludes the paper. This article is a shorter version of Chapter 2 presented in the PhD thesis [16].

Elias Bjørne*, Edmund Førland Brekke* and Tor Arne Johansen* are with the Centre for Autonomous Marine Operations and Systems, Department of Engineering Cybernetics, Norwegian University of Science and Technology (NTNU), NO-7491 Trondheim, Norway. (Email: elias.bjorne@itk.ntnu.no, edmund.brekke@ntnu.no, torleiv.h.bryne@ntnu.no, tor.arne.johansen@itk.ntnu.no).

II. NOTATION AND PRELIMINARIES

A. Notation

Scalars are lower case letters such as a, x, ω, vectors are lower case bold $\boldsymbol{a}, \boldsymbol{x}, \boldsymbol{\omega}$, sets are upper case A, X, Ω, and matrices are upper case bold $\boldsymbol{A}, \boldsymbol{X}, \boldsymbol{\Omega}$. The 0 denotes the scalar zero, while $\mathbf{0}$ is the matrix zero where dimensions are implicitly given by the context. The accents $\hat{\bullet}, \tilde{\bullet}, \dot{\bullet}, \bar{\bullet}, \underline{\bullet}$, denotes estimate, estimation error, time derivative, upper and lower bound respectively. The subscript $\bullet_{(m)}$ denotes the measured value. Some common mathematical expressions which will be used are: The Euclidean norm for vectors and Frobenius norm for matrices, denoted $\| \bullet \|$, absolute value, denoted $| \bullet |$ and the transpose, denoted $\bullet^\top$.

A vector can be represented in different coordinate systems. The representation is denoted with the superscripts $\bullet^b, \bullet^n$ which represents the body-fixed and earth-fixed (inertial) coordinate systems, respectively, and will be called body-frame and inertial-frame. Lower case will denote the indices of a landmark, vector or matrix $\bullet_i$ and $\bullet_{i,j}$.

B. Rotation representation

Rotation is the attitude change between two coordinate systems, and a rotation from coordinate system b to n is denoted with subscript $\bullet_{nb}$. This can be represented as Euler angles

$$\boldsymbol{\theta}_{nb} = [\phi, \theta, \psi]^\top \in \{\mathbb{R}^3 |\ |\phi| \leq \pi,\ |\theta| \leq \pi,\ |\psi| \leq \pi\}$$

and rotation matrix

$$\boldsymbol{\mathcal{R}}_{nb} \in \{\mathbb{R}^{3\times 3} |\ \boldsymbol{\mathcal{R}}_{nb}\boldsymbol{\mathcal{R}}_{nb}^\top = \boldsymbol{I}, \det(\boldsymbol{\mathcal{R}}_{nb}) = 1\} = SO(3)$$

The rotational vector transformation is calculated with the rotation matrix $\boldsymbol{x}^n = \boldsymbol{\mathcal{R}}_{nb}\boldsymbol{x}^b$.

The dynamics of the rotation matrix is described by

$$\dot{\boldsymbol{\mathcal{R}}}_{nb} = \boldsymbol{\mathcal{R}}_{nb}\boldsymbol{S}(\boldsymbol{\omega}) \tag{1}$$

where $\boldsymbol{\omega} = \boldsymbol{\omega}^b_{nb}$ is the angular velocity of the frame b relative to n decomposed in b. The matrix $\boldsymbol{S}(\boldsymbol{\omega})$, is the skew-symmetric matrix

$$\boldsymbol{S}(\boldsymbol{x}) = \begin{bmatrix} 0 & -x_3 & x_2 \\ x_3 & 0 & -x_1 \\ -x_2 & x_1 & 0 \end{bmatrix} \tag{2}$$

which formalizes how the cross product is performed through matrix multiplication $\boldsymbol{S}(\boldsymbol{x})\boldsymbol{y} = \boldsymbol{x} \times \boldsymbol{y}$. This matrix has several properties, such as: $\boldsymbol{S}(\bullet) = -\boldsymbol{S}(\bullet)^\top, \boldsymbol{x}^\top\boldsymbol{S}(\bullet)\boldsymbol{x} = \boldsymbol{0},\ \forall \boldsymbol{x} \in \mathbb{R}^3,\ \boldsymbol{S}(\boldsymbol{x})\boldsymbol{y} = -\boldsymbol{S}(\boldsymbol{y})\boldsymbol{x}$ and $\boldsymbol{\mathcal{R}}\boldsymbol{S}(\boldsymbol{x})\boldsymbol{\mathcal{R}}^\top = \boldsymbol{S}(\boldsymbol{\mathcal{R}}\boldsymbol{x}),\ \forall \boldsymbol{\mathcal{R}} \in SO(3)$. Moreover, the cross-product gives the difference in angle-axis between two vectors

$$\boldsymbol{S}(\boldsymbol{x})\boldsymbol{y} = \|\boldsymbol{x}\|\|\boldsymbol{y}\|\sin(\theta)\boldsymbol{u} \tag{3}$$

where θ is the angle between the vectors, and $\boldsymbol{u}$ is the unit vector of the axis of the rotation, defined by the right hand rule, and is orthogonal to $\boldsymbol{x}$ and $\boldsymbol{y}$. More detailed information can be found in [16].

A common source of error in attitude estimation is a gyro measurement

$$\boldsymbol{\omega}_m = \boldsymbol{\omega} + \boldsymbol{b}_\omega \tag{4}$$

that is corrupted by a gyro bias $\boldsymbol{b}_\omega$ that often needs to be estimated along with the attitude. The estimate of the rotation matrix is denoted $\hat{\boldsymbol{\mathcal{R}}}_{nb}$, and the error is defined by $\tilde{\boldsymbol{\mathcal{R}}}_{nb} = \hat{\boldsymbol{\mathcal{R}}}_{nb}\boldsymbol{\mathcal{R}}^\top_{nb}$ as in [17]. This means the error is a rotation matrix in itself.

C. Projection

It is useful to project vectors into the parallel and orthogonal spaces of a certain vector. This can be done using the unit vector $\boldsymbol{u}^n_x = \frac{\boldsymbol{x}}{\|\boldsymbol{x}\|}$ and skew symmetric matrices. We define the parallel and orthogonal projection matrices

$$\boldsymbol{U}^\perp_x = -\boldsymbol{S}(\boldsymbol{u}^n_{\boldsymbol{x}})^2 = \boldsymbol{I} - \boldsymbol{u}^n_{\boldsymbol{x}}(\boldsymbol{u}^n_{\boldsymbol{x}})^\top \tag{5}$$

$$\boldsymbol{U}^\parallel_x = \boldsymbol{u}^n_{\boldsymbol{x}}(\boldsymbol{u}^n_{\boldsymbol{x}})^\top \tag{6}$$

where the projection is performed by multiplying these matrices with the vector

$$\boldsymbol{U}^\perp_x\boldsymbol{y} \text{ is } \perp \text{ to } \boldsymbol{x}\ ,\ \boldsymbol{U}^\parallel_x\boldsymbol{y} \text{ is } \parallel \text{ to } \boldsymbol{x} \tag{7}$$

$$\boldsymbol{y} = \boldsymbol{U}^\perp_x\boldsymbol{y} + \boldsymbol{U}^\parallel_x\boldsymbol{y} \tag{8}$$

D. Landmark and vehicle dynamics

We assume that there is a vehicle with position $\boldsymbol{p}^n$ and m stationary landmarks where the ith landmark has position $\boldsymbol{p}^n_i$. The vectors to the landmarks are $\boldsymbol{\delta}^n_i = \boldsymbol{p}^n_i - \boldsymbol{p}^n$. These vectors can be represented by their range and bearing,

$$\varrho_i = \|\boldsymbol{\delta}^n_i\|\ ,\ \boldsymbol{u}^n_{\delta i} = \boldsymbol{\delta}^n_i/\|\boldsymbol{\delta}^n_i\| \tag{9}$$

where the range ϱ_i is the geometric distance, while the bearing vector $\boldsymbol{u}^n_{\delta i}$ is the unit vector pointing at the landmark. These can also be represented in the body-frame

$$\boldsymbol{\delta}^b_i = \boldsymbol{\mathcal{R}}^\top_{nb}\boldsymbol{\delta}^n_i,\quad \boldsymbol{u}^b_{\delta i} = \boldsymbol{\mathcal{R}}^\top_{nb}\boldsymbol{u}^n_{\delta i} \tag{10}$$

The kinematics of the position of the vehicle is

$$\dot{\boldsymbol{p}^n} = \boldsymbol{v}^n = \boldsymbol{\mathcal{R}}_{nb}\boldsymbol{v}^b \tag{11}$$

which implies $\dot{\boldsymbol{\delta}^n_i} = -\boldsymbol{v}^n$, which is used to find the time derivative in body-frame, from (1) and (10)-(11).

$$\begin{aligned}\dot{\boldsymbol{\delta}}^b_i &= \dot{\boldsymbol{\mathcal{R}}}^\top_{nb}\boldsymbol{\delta}^n_i + \boldsymbol{\mathcal{R}}^\top_{nb}\dot{\boldsymbol{\delta}}^n_i \\ &= (\boldsymbol{\mathcal{R}}_{nb}\boldsymbol{S}(\boldsymbol{\omega}))^\top\boldsymbol{\delta}^n_i + \boldsymbol{\mathcal{R}}^\top_{nb}(-\boldsymbol{v}^n) = -\boldsymbol{S}(\boldsymbol{\omega})\boldsymbol{\delta}^b_i - \boldsymbol{v}^b\end{aligned} \tag{12}$$

From this, the dynamics of the range and bearing vector can be found

$$2\dot{\varrho}_i\varrho_i = 2(\boldsymbol{\delta}^n_i)^\top\dot{\boldsymbol{\delta}}^n_i \tag{13}$$

$$\dot{\varrho}_i = (\boldsymbol{u}^n_{\delta i})^\top(-\boldsymbol{v}^n) = -(\boldsymbol{u}^n_{\delta i})^\top\boldsymbol{v}^n = -(\boldsymbol{u}^b_{\delta i})^\top\boldsymbol{v}^b \tag{14}$$

$$\begin{aligned}\dot{\boldsymbol{u}}^n_{\delta i} &= \boldsymbol{\delta}^n_i\frac{d}{dt}(\frac{1}{\varrho_i}) + \frac{\dot{\boldsymbol{\delta}}^n_i}{\varrho_i} = \boldsymbol{\delta}^n_i\frac{-1}{\varrho_i^2}\dot{\varrho}_i + \frac{-\boldsymbol{v}^n}{\varrho_i} \\ &= \frac{1}{\varrho_i}(\boldsymbol{u}^n_{\delta i}(\boldsymbol{u}^n_{\delta i})^\top - \boldsymbol{I})\boldsymbol{v}^n = \frac{1}{\varrho_i}\boldsymbol{S}(\boldsymbol{u}^n_{\delta i})^2\boldsymbol{v}^n\end{aligned} \tag{15}$$

$$\begin{aligned}\dot{\boldsymbol{u}}^b_{\delta i} &= \boldsymbol{\delta}^b_i\frac{d}{dt}(\frac{1}{\varrho_i}) + \frac{\dot{\boldsymbol{\delta}}^b_i}{\varrho_i} = \boldsymbol{\delta}^b_i\frac{-1}{\varrho^2}\dot{\varrho}_i + \frac{-S(\boldsymbol{\omega})\boldsymbol{\delta}^b_i - \boldsymbol{v}^b}{\varrho_i} \\ &= -\boldsymbol{S}(\boldsymbol{\omega})\boldsymbol{u}^b_{\delta i} + \frac{1}{\varrho_i}\boldsymbol{S}(\boldsymbol{u}^b_{\delta i})^2\boldsymbol{v}^b\end{aligned} \tag{16}$$

where $\boldsymbol{S}(\boldsymbol{u}^b_{\delta i})^2 = \boldsymbol{u}^b_{\delta i}(\boldsymbol{u}^b_{\delta i})^\top - \boldsymbol{I}$ is used. For mathematical convenience, the inverse range $d_i = \frac{1}{\varrho_i}$ is introduced, and (14) leads to

$$\dot{d}_i = -\frac{1}{\varrho_i^2}\dot{\varrho}_i = d_i^2(\boldsymbol{u}^n_{\delta i})^\top\boldsymbol{v}^n = d_i^2(\boldsymbol{u}^b_{\delta i})^\top\boldsymbol{v}^b \tag{17}$$

III. OBSERVER DESIGN

The proposed observer is a high gain observer resembling the dynamics of the bearing vector. It uses the velocity and gyro measurements to propagate and filter the bearing vector estimates while estimating both the inverted range to the landmarks and the gyro bias. The observer has body velocity $\boldsymbol{v}^b$, bearing vector $\boldsymbol{u}^b_{\delta i}$ and biased angular rate $\boldsymbol{\omega}_m$ as measurements. The bearing vector $\hat{\boldsymbol{u}}^b_{\delta i}$, inverted range to landmark $\hat{d}_i$ and gyro bias $\hat{\boldsymbol{b}}_\omega$ are estimated as follows

$$\dot{\hat{\boldsymbol{u}}}^b_{\delta i} = -\boldsymbol{S}(\boldsymbol{\omega}_m - \hat{\boldsymbol{b}}_\omega + k_i\boldsymbol{\sigma}_i + \hat{d}_i\boldsymbol{S}(\boldsymbol{u}^b_{\delta i})\boldsymbol{v}^b)\hat{\boldsymbol{u}}^b_{\delta i} \tag{18}$$

$$\begin{aligned}\dot{\hat{d}}_i &= \text{Proj}_{di}(\hat{d}_i^2(\boldsymbol{u}^b_{\delta i})^\top\boldsymbol{v}^b) \\ &\quad + k_{di}\text{Proj}_{di}((\boldsymbol{v}^b)^\top\boldsymbol{S}(\boldsymbol{u}^b_{\delta i})^2\boldsymbol{S}(\hat{\boldsymbol{u}}^b_{\delta i})\boldsymbol{\sigma}_i))\end{aligned} \tag{19}$$

$$\dot{\hat{\boldsymbol{b}}}_\omega = \boldsymbol{K}_b\text{Proj}_b(\sum_{i=1}^{m}\boldsymbol{S}(\hat{\boldsymbol{u}}^b_{\delta i})\boldsymbol{S}(\boldsymbol{u}^b_{\delta i})\boldsymbol{\sigma}_i) \tag{20}$$

$$\boldsymbol{\sigma}_i = \boldsymbol{S}(\boldsymbol{u}^b_{\delta i})\hat{\boldsymbol{u}}^b_{\delta i} \tag{21}$$

where $k_i > 0$, $k_{di} > 0$ and $\boldsymbol{K}_b > 0$ are gains. The $\text{Proj}_\bullet$ operator is presented in [16], and ensures that the bias estimate is maintained in a ball which is predefined, and that

the inverse range estimates are kept between $\underline{d} < \hat{d}_i < \bar{d}$. We see that $(\hat{\boldsymbol{u}}^b_{\delta i})^\top \dot{\hat{\boldsymbol{u}}}^b_{\delta i} = 0$, because $(\hat{\boldsymbol{u}}^b_{\delta i})^\top \boldsymbol{S}(\hat{\boldsymbol{u}}^b_{\delta i}) = \boldsymbol{0}$, which ensures that $\hat{\boldsymbol{u}}^b_{\delta i}$ is maintained on the unit ball.

First the error dynamics of $\tilde{\boldsymbol{u}}^b_{\delta i} = \boldsymbol{S}(\boldsymbol{u}^b_{\delta i})\hat{\boldsymbol{u}}^b_{\delta i} = \boldsymbol{\sigma}_i$, $\tilde{d}_i = d_i - \hat{d}_i$ and $\tilde{\boldsymbol{b}}_\omega = \boldsymbol{b}_\omega - \hat{\boldsymbol{b}}_\omega$ are derived:

$$\begin{aligned}\dot{\tilde{\boldsymbol{u}}}^b_{\delta i} &= \boldsymbol{S}(\boldsymbol{u}^b_{\delta i})\dot{\hat{\boldsymbol{u}}}^b_{\delta i} - \boldsymbol{S}(\hat{\boldsymbol{u}}^b_{\delta i})\dot{\boldsymbol{u}}^b_{\delta i}\\ \dot{\tilde{\boldsymbol{u}}}^b_{\delta i} &= \boldsymbol{S}(\tilde{\boldsymbol{u}}^b_{\delta i})\boldsymbol{\omega} + k_i \boldsymbol{S}(\boldsymbol{u}^b_{\delta i})\boldsymbol{S}(\hat{\boldsymbol{u}}^b_{\delta i})\tilde{\boldsymbol{u}}^b_{\delta i} + \boldsymbol{S}(\boldsymbol{u}^b_{\delta i})\boldsymbol{S}(\hat{\boldsymbol{u}}^b_{\delta i})\tilde{\boldsymbol{b}}_\omega\\ &\quad - \tilde{d}_i \boldsymbol{S}(\hat{\boldsymbol{u}}^b_{\delta i})\boldsymbol{S}(\boldsymbol{u}^b_{\delta i})\boldsymbol{S}(\boldsymbol{u}^b_{\delta i})\boldsymbol{v}^b + \hat{d}_i \boldsymbol{S}(\tilde{\boldsymbol{u}}^b_{\delta i})\boldsymbol{S}(\boldsymbol{u}^b_{\delta i})\boldsymbol{v}^b\end{aligned}$$

For details see [16]. We then end up with the error dynamics

$$\begin{aligned}\dot{\tilde{\boldsymbol{u}}}^b_{\delta i} &= [-\boldsymbol{S}(\hat{d}_i \boldsymbol{S}(\boldsymbol{u}^b_{\delta i})\boldsymbol{v}^b + \boldsymbol{\omega}) + k_i \boldsymbol{S}(\boldsymbol{u}^b_{\delta i})\boldsymbol{S}(\hat{\boldsymbol{u}}^b_{\delta i})]\tilde{\boldsymbol{u}}^b_{\delta i}\\ &\quad + \boldsymbol{S}(\boldsymbol{u}^b_{\delta i})\boldsymbol{S}(\hat{\boldsymbol{u}}^b_{\delta i})\tilde{\boldsymbol{b}}_\omega - \boldsymbol{S}(\hat{\boldsymbol{u}}^b_{\delta i})\boldsymbol{S}(\boldsymbol{u}^b_{\delta i})^2\boldsymbol{v}^b\tilde{d}_i \qquad (22)\\ \dot{\tilde{d}}_i &= -k_{di}\text{Proj}_{di}\left((\boldsymbol{v}^b)^\top \boldsymbol{S}(\boldsymbol{u}^b_{\delta i})^2 \boldsymbol{S}(\hat{\boldsymbol{u}}^b_{\delta i})\tilde{\boldsymbol{u}}^b_{\boldsymbol{\delta i}}\right)\\ &\quad + d_i^2(\boldsymbol{u}^b_{\delta i})^\top \boldsymbol{v}^b + \text{Proj}_{di}\left(-\hat{d}_i^2(\boldsymbol{u}^b_{\delta i})^\top \boldsymbol{v}^b\right) \qquad (23)\\ \dot{\tilde{\boldsymbol{b}}}_\omega &= -\boldsymbol{K}_b \text{Proj}_b\Big(\sum_{i=1}^m \boldsymbol{S}(\hat{\boldsymbol{u}}^b_{\delta i})\boldsymbol{S}(\boldsymbol{u}^b_{\delta i})\tilde{\boldsymbol{u}}^b_{\delta i}\Big) \qquad (24)\end{aligned}$$

by assuming that the bias is constant $\dot{\boldsymbol{b}}_\omega = \boldsymbol{0}$. We see that the error dynamics has an equilibrium for $\tilde{\boldsymbol{u}}^b_{\delta i} = \boldsymbol{0}$, $\tilde{d}_i = 0$ and $\tilde{\boldsymbol{b}}_\omega = \boldsymbol{0}$. In addition, we stack the bearing errors in the vector $\boldsymbol{x} = [(\tilde{\boldsymbol{u}}^b_{\delta 1})^\top, \cdots, (\tilde{\boldsymbol{u}}^b_{\delta m})^\top]^\top$, and the inverted range estimation errors and gyro bias error in vector $\boldsymbol{y} = [\tilde{d}_1, \cdots, \tilde{d}_m, (\tilde{\boldsymbol{b}}_\omega)^\top]^\top$. The structure of the error dynamics can then be represented as

$$\dot{\boldsymbol{x}} = \boldsymbol{\mathcal{A}}(t)\boldsymbol{x} + \boldsymbol{\mathcal{B}}(t)\boldsymbol{y} \qquad (25)$$

$$\dot{\boldsymbol{y}} = -\boldsymbol{\Gamma}\boldsymbol{\mathcal{B}}_p(t,\boldsymbol{x})^\top + \boldsymbol{g}(t,\boldsymbol{y}) \qquad (26)$$

where the matrices are defined as

$$\begin{aligned}&\boldsymbol{\mathcal{A}}(t) =\\ &\text{diag}(\{-\boldsymbol{S}(\hat{d}_i \boldsymbol{S}(\boldsymbol{u}^b_{\delta i})\boldsymbol{v}^b + \boldsymbol{\omega}) + k_i \boldsymbol{S}(\boldsymbol{u}^b_{\delta i})\boldsymbol{S}(\hat{\boldsymbol{u}}^b_{\delta i})\}_{i=1}^m)\\ &\boldsymbol{\mathcal{B}}(t) =\\ &\begin{bmatrix}\text{diag}(\{-\boldsymbol{S}(\hat{\boldsymbol{u}}^b_{\delta i})\boldsymbol{S}(\boldsymbol{u}^b_{\delta i})^2\boldsymbol{v}^b\}_{i=1}^m) & \{\boldsymbol{S}(\boldsymbol{u}^b_{\delta i})\boldsymbol{S}(\hat{\boldsymbol{u}}^b_{\delta i})\}_{i=1}^m\end{bmatrix}\\ &\boldsymbol{\mathcal{B}}_p(t,\boldsymbol{x})^\top = \begin{bmatrix}\left\{\text{Proj}_{di}\left((\boldsymbol{v}^b)^\top \boldsymbol{S}(\boldsymbol{u}^b_{\delta i})^2\boldsymbol{S}(\hat{\boldsymbol{u}}^b_{\delta i})\tilde{\boldsymbol{u}}^b_{\delta i}\right)\right\}_{i=1}^m\\ \text{Proj}_b\left(\sum_{i=1}^m \boldsymbol{S}(\hat{\boldsymbol{u}}^b_{\delta i})\boldsymbol{S}(\boldsymbol{u}^b_{\delta i})\tilde{\boldsymbol{u}}^b_{\delta i}\right)\end{bmatrix}\end{aligned}$$

where $\{\bullet_i\}_1^m = [(\bullet_i|_{i=1})^\top, \cdots, (\bullet_i|_{i=m})^\top]^\top$ is a column vector or a matrix, where the entries $\bullet_i$ are stacked above each-other. The gain matrix is

$$\boldsymbol{\Gamma} = \begin{bmatrix}\text{diag}(k_{d1}, \cdots, k_{dm}) & \boldsymbol{0}\\ \boldsymbol{0} & \boldsymbol{K}_b\end{bmatrix} \qquad (27)$$

where we see that $\boldsymbol{\Gamma}$ is positive definite with a smallest and largest eigenvalues $\bar{\gamma}, \underline{\gamma}$, which also gives bounds on the observer gains. Finally,

$$\boldsymbol{g}(t,\boldsymbol{y}) = \begin{bmatrix}\left\{d_i^2(\boldsymbol{u}^b_{\delta i})^\top \boldsymbol{v}^b + \text{Proj}_{di}\left(-\hat{d}_i^2(\boldsymbol{u}^b_{\delta i})^\top \boldsymbol{v}^b\right)\right\}_1^m\\ \boldsymbol{0}\end{bmatrix}$$

We use this notation to highlight the similarities between $\boldsymbol{\mathcal{B}}_p(t,\boldsymbol{x})^\top$ and $\boldsymbol{\mathcal{B}}(t)^\top\boldsymbol{x}$ which in fact are identical $\boldsymbol{\mathcal{B}}_p(t,\boldsymbol{x})^\top = \boldsymbol{\mathcal{B}}(t)^\top\boldsymbol{x}$ when there are no projections activated. This notation helps the reader to see why the adaptation law of the inverted range and gyro bias were chosen i.e. to relate the system to the family of skew-symmetric systems that have been investigated extensively in many forms, including [18], [19], [20], [21]. In the first lemma we show that the persistence of excitation (PE) condition of this system related to the skew-symmetric part can be checked with a simpler matrix inequality.

Lemma 1: Consider the matrix $\boldsymbol{\mathcal{B}}(t)$, representing the part of the dynamic (25) that is linearly dependent on $\boldsymbol{y}$. Assume velocity of the vehicle is non-zero, $\|\boldsymbol{v}^b\| > 0$, not parallel to the bearing measurements, and there are at least three bearing measurements that are linearly independent so that the following inequalities hold

$$-(\boldsymbol{v}^b)^\top \boldsymbol{S}(\boldsymbol{u}^b_{\boldsymbol{\delta i}})^{\boldsymbol{2}}\boldsymbol{S}(\hat{\boldsymbol{u}}^b_{\boldsymbol{\delta i}})^{\boldsymbol{2}}\boldsymbol{S}(\boldsymbol{u}^b_{\boldsymbol{\delta i}})^{\boldsymbol{2}}\boldsymbol{v}^{\boldsymbol{b}} > \underline{\text{a}}\ ,\ \forall i \qquad (28)$$

$$-\sum_{i=1}^m \frac{1}{\boldsymbol{\xi_i}^\top \boldsymbol{\xi_i}}\boldsymbol{S}(\hat{\boldsymbol{u}}^b_{\delta i})\boldsymbol{S}(\boldsymbol{u}^b_{\delta i})\boldsymbol{S}(\boldsymbol{\xi_i})\boldsymbol{S}(\boldsymbol{\xi_i})\boldsymbol{S}(\boldsymbol{u}^b_{\delta i})\boldsymbol{S}(\hat{\boldsymbol{u}}^b_{\delta i}) > \underline{\text{b}} \qquad (29)$$

$$\boldsymbol{\xi_i} = -\boldsymbol{S}(\hat{\boldsymbol{u}}^b_{\delta i})\boldsymbol{S}(\boldsymbol{u}^b_{\delta i})^2\boldsymbol{v}^b \qquad (30)$$

where $\underline{\text{a}} > 0$ and $\underline{\text{b}} > 0$ are lower bounds. Then the matrix

$$\boldsymbol{\mathcal{B}}(t)^\top\boldsymbol{\mathcal{B}}(t) > \mu\boldsymbol{I} \qquad (31)$$

is positive definite, where $\mu > 0$ is a lower bound.

Proof: The details of the proof can be seen in Chapter 3 of [16], which is based on deriving the Schur complement of $\boldsymbol{\mathcal{B}}(t)^\top\boldsymbol{\mathcal{B}}(t)$, which leads to the expressions (28)-(29). ■

The first inequality (28) intuitively makes sense, since the range to the landmark is unobservable if the bearing is parallel to the velocity, hence constant. This is similar to what is found in [7], [9], [11], [12], where the derivative of the bearing vector being nonzero is a necessary condition for PE and observability. What distinguishes the presented observer from these, is that gyro bias estimation is also performed. In addition, the landmark positions are estimated, which is not done in [9], [22].

The condition of having (28) satisfied for every bearing is to guarantee that all inverted range estimates converge. In simulations, violating this condition for some time or initializing the bearing vector estimate parallel to the velocity vector did not cause any problem for the observer. In addition, as we will see in experiments, this condition will not be necessary to make the gyro-bias estimation converge.

The second inequality (29) is less intuitive. We see that for the matrix to be positive definite, we need that at least three bearing vectors exist, in which the projection of the velocity onto their orthogonal space spans $\mathbb{R}^3$ at all time

$$\exists i,j,k \in \{1,m\}|\text{span}([\boldsymbol{U}^\perp_{\delta^b_i}\boldsymbol{v}^b,\ \boldsymbol{U}^\perp_{\delta^b_j}\boldsymbol{v}^b,\ \boldsymbol{U}^\perp_{\delta^b_k}\boldsymbol{v}^b]) = \mathbb{R}^3$$

This gives us the intuition that the value μ in (31) will be related to how different the bearing vectors are, and how aligned they are to the velocity vector.

Remark 1: For the special case when velocity is zero, the inverse range d_i is unobservable, and can be neglected.

To show that the gyro bias can be estimated, set $\boldsymbol{y} = \tilde{\boldsymbol{b}}_\omega$, yielding $\boldsymbol{\mathcal{B}}(t) = \{\boldsymbol{S}(\boldsymbol{u}^b_{\delta i})\boldsymbol{S}(\hat{\boldsymbol{u}}^b_{\delta i})\}_i^m$, $\boldsymbol{\mathcal{B}}(t)^\top\boldsymbol{\mathcal{B}}(t) = -\sum_{i=1}^m \boldsymbol{S}(\hat{\boldsymbol{u}}^b_{\delta i})\boldsymbol{S}(\boldsymbol{u}^b_{\delta i})\boldsymbol{S}(\boldsymbol{u}^b_{\delta i})\boldsymbol{S}(\hat{\boldsymbol{u}}^b_{\delta i})$ and $\boldsymbol{g}(t,\boldsymbol{y}) = 0$. The system is skew symmetric without pertubation and can be shown to be uniformally semi-globally asymotically and locally exponentially stable using similar steps as in the proof of Theorem 1.

The following theorem says that a high gain can be chosen so that the system is uniformly semi-globally asymptotically stable, and exponentially stable in the large.

Theorem 1: Consider the kinematics of a vehicle where bearing of landmarks $\boldsymbol{u}^b_{\delta i}$, velocity $\boldsymbol{v}^b$, and biased angular rate $\boldsymbol{\omega}_m$ are measured, and assume that all inputs and system functions are Lipschitz and bounded. Further we assume that the landmarks are a minimum distance away from the vehicle so that the inverted ranges are also bounded. If we choose gains k_i large enough, then there exist gains k_{di} and $\boldsymbol{K}_b$ such that the error dynamic of the observer (18)-(20) converges in finite time from initial estimates $\hat{\boldsymbol{u}}^n_{\delta i}$ satisfying $(\hat{\boldsymbol{u}}^b_{\delta i})^\top \boldsymbol{u}^b_{\delta i} > \cos(\pi - \epsilon)$, and the origin is exponentially stable for $(\hat{\boldsymbol{u}}^b_{\delta i})^\top \boldsymbol{u}^b_{\delta i} > \cos(\epsilon)$ as long as the assumptions of Lemma 1 are fulfilled, where $\epsilon > 0$ is an arbitrary small constant.

Outline of the proof:

A) First prove that the the system (18)-(20) is Uniformly Bounded (UB), and the error states converges to an open set.
B) Define a Lyapunov function candidate for the error dynamics (22)-(24) and find its time derivative. Derive bounds on the terms of the time derivative.
C) Handle the projection related to the perturbation terms, and derive a bound on the perturbation.
D) Using bounds B) and C), to show that there exist gains that yields exponential stability in the large.
E) Combine A), D) to conclude that the observer is semi-globally asymptotically stable.

The proof can be seen in Chapter 3 of [16], where lower bounds on the gain k_i are given.

A. Decoupling of gyro bias estimation

Remark 2: It should be noted that inertial/body reference vectors, such as magnetometer and gravity, can also be used in the gyro bias observer, where the vectors can be included by using $\boldsymbol{u}^b_{\delta i} = \boldsymbol{r}^b_i$ and by setting $d_i = \hat{d}_i = 0$, and thus annihilate its effect.

As will be seen later in the article, the rate of convergence of the gyro bias estimation error can be quite different in different axes. This affects how large gain one might desire to have for the gyro bias estimation in different directions. An example of this is when a reference vector $\boldsymbol{r}^b$ is significant. Since this reference vector makes the gyro bias with axis orthogonal to this vector more available, it can be desirable to divide the gyro bias estimation into the space orthogonal $\boldsymbol{r}^{b\perp}$ and parallel $\boldsymbol{r}^{b\parallel}$ to this vector. We recall the projection transformations

$$\boldsymbol{U}^\perp_r = -\boldsymbol{S}(\boldsymbol{r}^b)^2 \ , \ \boldsymbol{U}^\parallel_r = \boldsymbol{r}^b(\boldsymbol{r}^b)^\top \tag{32}$$

This can then be used to provide one gain for the gyro bias estimation parallel to, and another gain for the bias estimation orthogonal to, the reference vector

$$\begin{aligned}
\dot{\hat{\boldsymbol{u}}}^b_{\delta i} &= -\boldsymbol{S}(\boldsymbol{\omega}_m - \hat{\boldsymbol{b}}_\omega + k_i\boldsymbol{\sigma}_i)\hat{\boldsymbol{u}}^b_{\delta i} + \hat{d}_i\boldsymbol{S}(\hat{\boldsymbol{u}}^b_{\delta i})\boldsymbol{S}(\boldsymbol{u}^b_{\delta i})\boldsymbol{v}^b \\
\dot{\hat{\boldsymbol{r}}}^b &= -\boldsymbol{S}(\boldsymbol{\omega}_m - \hat{\boldsymbol{b}}_\omega + k_r\boldsymbol{\sigma}_r)\hat{\boldsymbol{r}}^b \qquad (33)\\
\dot{\hat{d}}_i &= \text{Proj}_{di}(\hat{d}_i^2(\boldsymbol{u}^b_{\delta i})^\top\boldsymbol{v}^b) \\
&\quad + k_{di}\text{Proj}_{di}((\boldsymbol{v}^b)^\top\boldsymbol{S}(\boldsymbol{u}^b_{\delta i})^2\boldsymbol{S}(\hat{\boldsymbol{u}}^b_{\delta i})\boldsymbol{\sigma}_i) \qquad (34)\\
\dot{\hat{\boldsymbol{b}}}_\omega &= (k_{1b}\boldsymbol{U}^\parallel_r + k_{2b}\boldsymbol{U}^\perp_r)\text{Proj}_b(\sum_{i=1}^m(\boldsymbol{S}(\hat{\boldsymbol{u}}^b_{\delta i})\boldsymbol{S}(\boldsymbol{u}^b_{\delta i})\boldsymbol{\sigma}_i) \\
&\quad + \boldsymbol{S}(\hat{\boldsymbol{r}}^b)\boldsymbol{S}(\boldsymbol{r}^b)\boldsymbol{\sigma}_r) \qquad (35)\\
\boldsymbol{\sigma}_i &= \boldsymbol{S}(\boldsymbol{u}^b_{\delta i})\hat{\boldsymbol{u}}^b_{\delta i} \ , \ \boldsymbol{\sigma}_r = \boldsymbol{S}(\boldsymbol{r}^b)\hat{\boldsymbol{r}}^b \qquad (36)
\end{aligned}$$

The crucial part is that the gyro bias estimation can be tuned to balance the difference in the convergence rate. We believe that the reason for this difference in convergence rate along the different axis is related to the different eigenvalues of the matrix (29) which will be shown for different scenarios in the simulation example.

IV. SIMULATION RESULTS AND PERFORMANCE EVALUATION

One interesting question to investigate is how the landmark distribution will affect the convergence of the observer. Lemma 1 show that the convergence of the inverted distance estimate to the landmark depends on the velocity not being parallel to the landmark bearing, which is intuitive as the distance to the landmark is unobservable if the bearing measurement is stationary. This is consistent with the observability results and PE conditions found in [12], [11], [7], [9]. For the convergence of the gyro bias estimate, we see that it is related to the inequality

$$-\sum_{i=1}^m \frac{1}{\boldsymbol{\xi}^\top\boldsymbol{\xi}}\boldsymbol{S}(\hat{\boldsymbol{u}}^b_{\delta i})\boldsymbol{S}(\boldsymbol{u}^b_{\delta i})\boldsymbol{S}(\boldsymbol{\xi})\boldsymbol{S}(\boldsymbol{\xi})\boldsymbol{S}(\boldsymbol{u}^b_{\delta i})\boldsymbol{S}(\hat{\boldsymbol{u}}^b_{\delta i}) > \boldsymbol{0}$$

where we recall that $\boldsymbol{\xi} = -\boldsymbol{S}(\hat{\boldsymbol{u}}^b_{\delta i})\boldsymbol{S}(\boldsymbol{u}^b_{\delta i})^2\boldsymbol{v}^b$. To better understand this inequality, and how its positive definiteness depend on landmark positions, the related matrix

$$\sum_{i=1}^m \frac{1}{\hat{\boldsymbol{\xi}}^\top\hat{\boldsymbol{\xi}}}\boldsymbol{S}(\boldsymbol{u}^b_{\delta i})^2\boldsymbol{S}(\hat{\boldsymbol{\xi}})\boldsymbol{S}(\hat{\boldsymbol{\xi}})\boldsymbol{S}(\boldsymbol{u}^b_{\delta i})^2 \tag{37}$$

$$\hat{\boldsymbol{\xi}} = -\boldsymbol{S}(\boldsymbol{u}^b_{\delta i})^3\boldsymbol{v}^b \tag{38}$$

was calculated, and its eigenvalues were compared in the different setups. We note that the matrix is independent of the range estimates, the angular rate, as well as the attitude and the magnitude of the velocity as long as it is non-zero. A scenario can be seen in Figure 1.

The matrix (37) and its eigenvalues were calculated for several consecutive scenarios where the virtual camera setup was varied with different number of bearing measurements, different angles between the velocity and the camera axis,

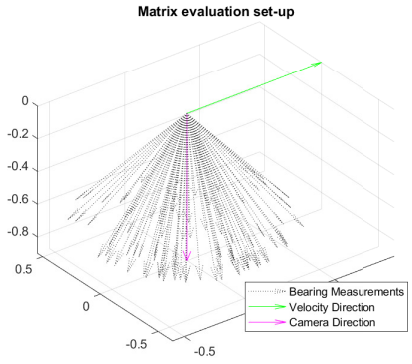

Fig. 1: Simulation setup for evaluating the matrix (37)

and different field of view (FOV) of the camera. For each parameter setup, the matrix was calculated 10 times with randomly bearings satisfying the the parameters. The eigenvalues of these matrices can be seen in Figure 2, where one can see how the camera position relative to the velocity affects the convergence of the gyro bias estimate. However, this example does not take into account the difference in noise that the bearing measurements experience because of changing FOV. Not surprisingly, having too narrow FOV will make gyro bias estimation difficult. From Figure 2a one can see that after having a FOV of 150^o, an increase in FOV will not make the eigenvalues more negative. For the case when the camera is looking in the same direction as the velocity, which is typical for an automotive application, see Figure 2b, the matrix has an optimal FOV close to 90^o. We see from Figure 2c that for a camera with 90^o FOV, the optimal angle between the camera and the velocity is 0^o, 60^o, 120^o and 180^o. It is also intresting to see from Figure 2d that the eigenvalues have a linear dependency with regards to the number of bearings.

A. UAV flight simulation

For the next simulation we have investigated a common setup for UAV camera navigation, where a UAV has a downward looking camera. From Figure 2a, we see that for the camera we are simulating, a 90^o FOV can be troublesome, as the movement of the UAV is often perpendicular to the camera direction. Nevertheless, we will show that the sensor setup presented in (33)-(36), will still give satisfactory results. The camera will work both as a gyro bias estimator, especially in yaw, as well as an estimate for range to landmarks which are seen. The setup was tested in simulations, where a vehicle is moving in a circle with radius of 10 m, looking downward at a plane from a height of 13 m. The simulation setup can be seen in Figure 3, where one can see that the landmarks dies and are born, and the number of bearing measurements varied between 166 to 215. When the estimates have converged and all innovations were kept under a threshold, a timer was introduced for accepting new landmarks/states so that they could converge before they affected the gyro bias estimate. This let the inverse range estimates converge before they affected the gyro bias

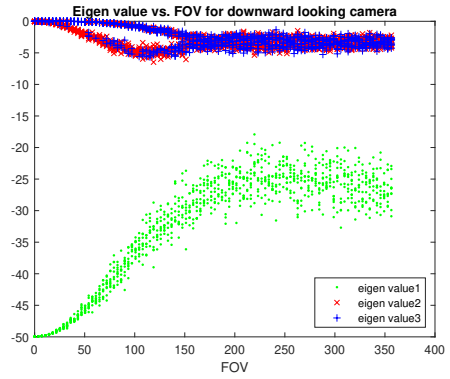

(a) Plotted against the FOV in the downward looking camera, with 50 bearing measurements.

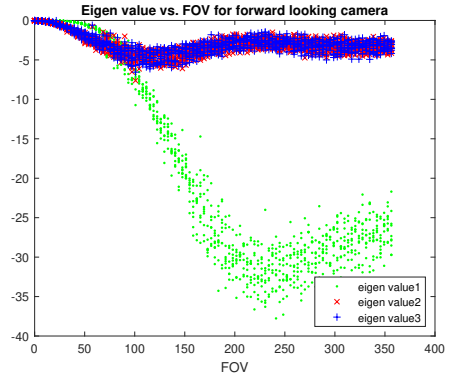

(b) Plotted against the FOV in the forward looking camera, with 50 bearing measurements.

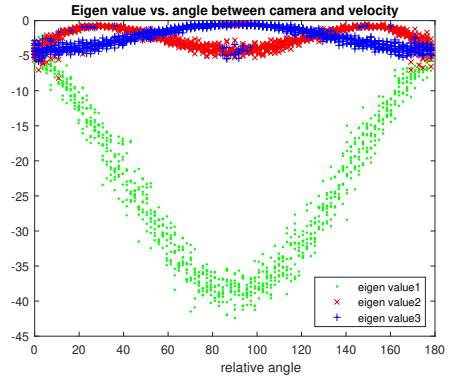

(c) Plotted against the angle between the camera and the velocity with FOV 90^o with 50 bearing measurements.

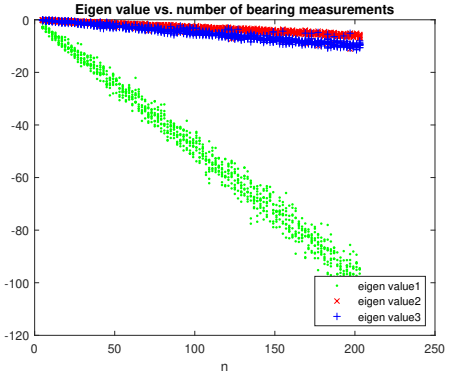

(d) Plottet against the number n of bearing measurements. The camera was pointed at 45^o forwards with regards to the velocity, and with a FOV of 90^o.

Fig. 2: The eigenvalues of matrix (37).

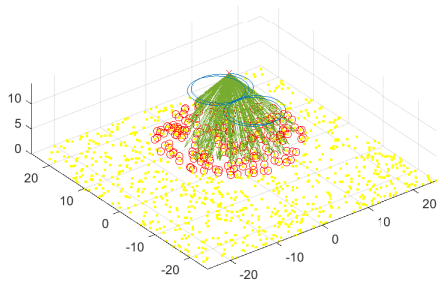

Fig. 3: The trajectory of the UAV with a downward looking camera. The red points are the landmarks that are observed by the camera, and the green arrows are the bearing measurements scaled according to the inverse range estimates.

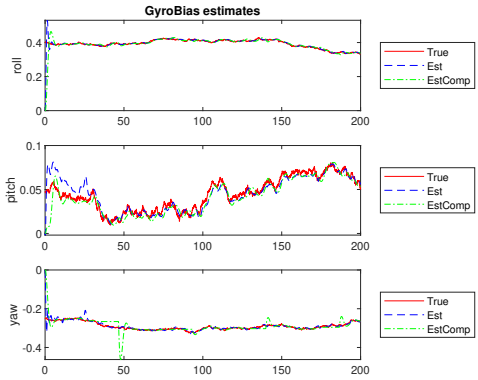

Fig. 4: The gyro bias estimation, where the true bias is propagated according to (39). The blue estimate is from the novel observer, while the green estimate is from the complimentary filter [15].

estimate. An extension of this could be to estimate whether a bearing measurement is PE, and let this influence the gains of the observer. However, for the scenarios encountered both in simulations and experiments, such a setup was not deemed necessary to achieve satisfactory results.

The simulator was discretized with the Euler method with step length $\Delta t = 0.067$, and white measurement and process noise were added. In addition a gyro measurement $\boldsymbol{\omega}_m$ had a bias that was initialized as $\boldsymbol{b}_\omega = [0.4,\ 0.05,\ -0.25]^\top$ and updated by a white noise with standard deviation $\sigma_{bw} = 0.001$ according to

$$\boldsymbol{b}_\omega(t + \Delta t) = \boldsymbol{b}_\omega(t) + \mathcal{N}(0, \sigma_{bw}^2) \tag{39}$$

In addition, the gyro measurement was corrupted with a white noise with standard deviation $\boldsymbol{\sigma}_\omega = 0.001 \cdot \boldsymbol{I}$. The noise of the bearing vector measurements were $\boldsymbol{\sigma}_u = 0.00314 \cdot \boldsymbol{I}$. The bearing vector noise was orthogonal to the bearing vector measurement $\boldsymbol{u}_{\delta i}^b = \boldsymbol{S}(\boldsymbol{u}_{\delta i}^b)\boldsymbol{w}_u$, where the noise $\boldsymbol{w}_u$ was a white noise vector $\boldsymbol{w}_u = \mathcal{N}(0, \boldsymbol{\sigma}_u^2)$. As the bearing vector is normalized the noise becomes nonlinear. The gravity was utilized as a reference vector

$$\boldsymbol{r}_1^n = [0,\ 0,\ -1]^\top,\ \boldsymbol{r}_1^b = \boldsymbol{f}_{imu}/\|\boldsymbol{f}_{imu}\| \tag{40}$$

where the IMU measures the specific force, $\boldsymbol{f}_{imu} = \boldsymbol{\mathcal{R}}_{nb}^\top(\boldsymbol{a}^n - \boldsymbol{g}^n + \boldsymbol{w}_f)$ and $\boldsymbol{w}_f = \mathcal{N}(0, \boldsymbol{I}\sigma_f^2)$ with $\sigma_f = 0.002$.

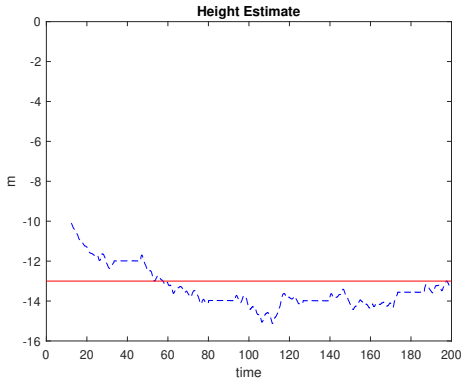

Fig. 5: The height estimate derived from the inverse range estimates compared to the truth.

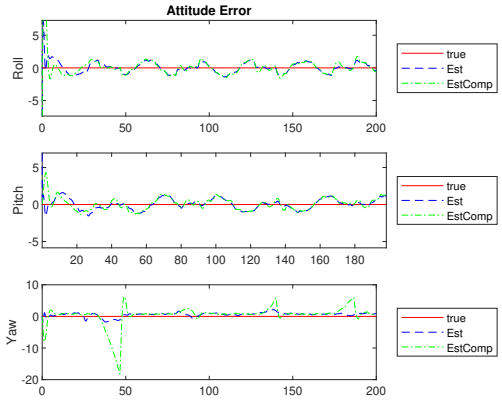

Fig. 6: The attitude estimates with the estimates from the complimentary filter from the simulations in degrees.

For the attitude estimate the GNSS and camera velocity were also used as a reference vector.

$$\boldsymbol{r}_2^n = (\boldsymbol{v}^n + \boldsymbol{w}_v)/\|\boldsymbol{v}^n + \boldsymbol{w}_v\| \tag{41}$$

$$\boldsymbol{r}_2^b = (\boldsymbol{v}_{cam}^b + \boldsymbol{w}_{vc})/\|\boldsymbol{v}_{cam}^b + \boldsymbol{w}_{vc}\| \tag{42}$$

where $\boldsymbol{v}_{cam}^b$ is the camera velocity, and $\boldsymbol{w}_v,\ w_{vc}$ is the GNSS and camera velocity noise vector with $\sigma_v = 0.05$ and $\sigma_{vc} = 0.05$. As a reference attitude observer we used the complimentary filter [15], with the same reference vectors.

The velocity was 1 [m/s] set to zero four times at $t = 33.3,\ 80.0,\ 126.7$ and 173.3 for 13.2 seconds. This to see how the observer setups reacted to having zero velocity. The gains used for the simulation was $k_i = 2\sqrt{0.9}, k_r = k_{di} = 0.9, \boldsymbol{k}_{1b} = \frac{1}{m}6, \boldsymbol{k}_{2b} = 1$ and were found through a combination of the tuning preformed in [23], and trial and error. From Figure 4, it can be seen that the observers are able to estimate the gyro bias quite accurately. In addition, it can be seen how the proposed observer is able handle zero velocity compared to the straight-forward velocity-based observer. Another benefit is also seen for the cascaded system, since the bias estimation is independent of the attitude estimate, and the error in the attitude does not affect the gyro bias estimation. It can also be seen how this affects the yaw estimates in Figure 6. In Figure 5, the height estimate acquired from the observer inverse range estimates are shown. For this setup, the height estimate is found by averaging the projected length estimates onto the

vertical unit vector $\hat{h} = \frac{1}{n(\mathcal{C})} \sum_{i \in \mathcal{C}} \frac{1}{\hat{d}} (\boldsymbol{r}^b)^\top \hat{\boldsymbol{l}}_i^b$ where the set $\mathcal{C}$ contains the indices of the estimates that are regarded as converged, meaning that the bearing error $\boldsymbol{\sigma}_{ui}$ has become sufficiently small. This is also a reason why there is no height estimate at the beginning, as it takes some time for the bearing estimates to converge. The cardinality of the set $\mathcal{C}$ is denoted $n(\mathcal{C})$. The estimate can hence be used to have a more accurate height estimate, without having to use pressure or laser altimeter together with the GNSS. From the simulations we see that the camera can both replace a pressure sensor and a magnetometer, assuming that a sufficient number of landmarks are detected.

V. EXPERIMENTAL VALIDATION

The experimental validation was carried out by using an octocopter flying in a circle with an autopilot for 150 seconds. The data set was recorded from a payload consisting of a SenTiBoard, a uBlox GNSS receiver and a STIM300 tactical grade MEMS IMU [24]. The SenTiBoard was also connected to the flash signal of a uEye UI-3140CP camera, time stamping the flash signal from the camera such that accurate timing of the images were available. The sensor data and images were stored using an Odroid UX4. Before the flight, the IMU, camera and temporal calibration was performed using the Kalibr toolbox [25], [26], finding IMU biases, time delay and coordinate transformation between the camera and the IMU. In the data set used in this article, the estimated image capture time delay was less than 3 ms, and as the timing of the image was measured by flash signal it was independent of the kernel load and thus assumed to be constant. As the IMU was tactical grade, the accelerometer and gyro biases were assumed constant for the duration of the experiment and respectively $\boldsymbol{b}_a = [0.03,\ 0.005,\ 0.085]^\top$ [m/s^2] and $\boldsymbol{b}_\omega = [0.007,\ -0.0002,\ 0.0017]^\top$ [rad/s]. The objective of the experiment was to verify that the observer could estimate a gyro bias, we added a synthetic gyro-bias following (39) with initial value $\check{\boldsymbol{b}}_\omega = [0.1,\ 0.4,\ -0.25]^\top$. Thus we could verify that the gyro bias estimated by the observer was equal to the synthetic one. The tuning parameters used in the experiments were $k_i = 2, k_r =, k_{di} = 1, \boldsymbol{k}_{1b} = \frac{1}{m}12, \boldsymbol{k}_{2b} = 2$.

As the experiments were performed while flying over flat fields, homography transformation between two images were used to acquire the camera velocity needed. For more detail on how this is done see [27]. For feature extraction we used Harris Min Eigen features [28] which was tracked with the Kanade-Lucas-Tomasi feature tracker [29]. The homography matrix was found with a 4-point direct linear transformation (DLT) [30] and outlier rejection was done using RANSAC. The velocity was extracted from the homography using techniques based on [31], this provided the camera velocity $\boldsymbol{v}^c_{hom} = \frac{\boldsymbol{v}^c}{h}$, which is divided by the height over the plane. The GNSS velocity was then used to scale the velocity so that the body velocity used in the observer was $\hat{\boldsymbol{v}}^b = \boldsymbol{\mathcal{R}}_{bc} \frac{\boldsymbol{v}^c_{hom}}{\|\boldsymbol{v}^c_{hom}\|} \|\boldsymbol{v}^n_{gnss}\|$, where the lever arm effects were neglected, and $\boldsymbol{\mathcal{R}}_{bc}$ is the rotation from camera to IMU. The trajectory of the position can be seen in Figure 7, where the number of bearing measurements varied between 317 to 410. From the plots, it is evident that the observer is also able to converge with experimental data. The gyro bias estimate seems to achieve acceptable accuracy, and the height estimate gives a reasonable estimate for the octocopter altitude over the ground. As in the simulations there seems to be some bias in the estimates. Nevertheless, this shows that applying the proposed observer together with a camera can give robust gyro bias estimation as well as a height estimate.

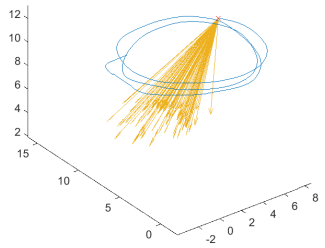

Fig. 7: The trajectory of the UAV with a downward looking camera. The yellow arrows are the bearing measurements scaled according to the inverse range estimates.

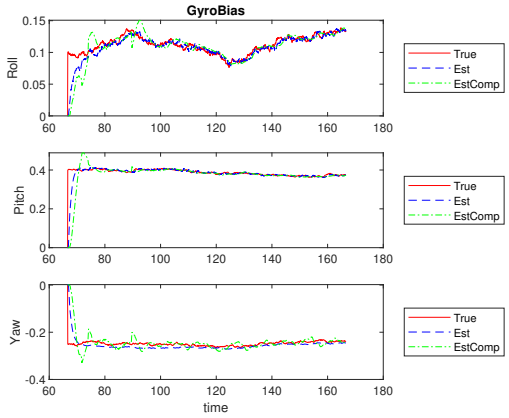

Fig. 8: The gyro bias estimation preformed by the novel observer and complimentary filter on experimental data.

VI. CONCLUSION

The article introduces a nonlinear observer that combines velocity, gyro and bearing measurements from landmarks

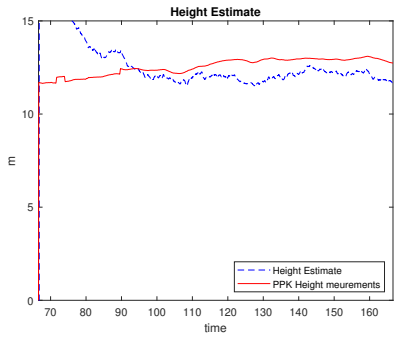

Fig. 9: The height estimate derived from the inverted range estimates compared with the post process kinematic (PPK) height estimate.

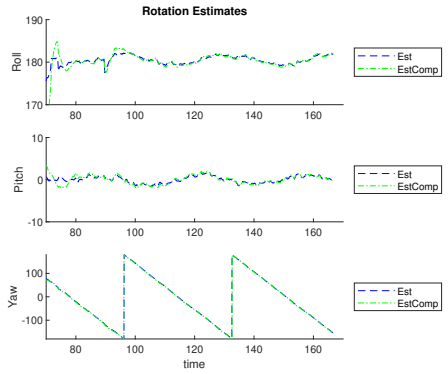

Fig. 10: The attitude estimate of the complimentary filter (EstComp) vs the cascade attitude setup (Est).

to estimate the distance to the landmarks as well as the gyro-bias and attitude. It was proven to be semi-globally asymptotically stable and exponentially stable in the large if a persistence of excitation condition holds. The observer was demonstrated in simulations and on experimental data, where it was shown how a camera could replace a magnetometer and altimeter.

It should also be noted that if GNSS is unavailable, the body velocity could be acquired with an altimeter or laser scanner which could be used for scaling the camera velocity, and thus the observer could be used for more accurate and drift free position estimates, similar to what was shown in [12]. If in addition it is combined with optimization [32] and an image to image loop closing system [13], the bearing only SLAM with semi global stability properties can be achieved.

ACKNOWLEDGEMENT

This work was supported by the Research Council of Norway project number 250725, and Centre for autonomous marine operations and systems, project number 223254.

REFERENCES

[1] T. Hamel and C. Samson, "Riccati observers for the nonstationary pnp problem," *IEEE Transactions on Automatic Control*, vol. 63, no. 3, pp. 726–741, 2017.

[2] A. I. Mourikis and S. I. Roumeliotis, "A Multi-State Constraint Kalman Filter for Vision-aided Inertial Navigation," in *Proceedings 2007 IEEE International Conference on Robotics and Automation*, (Rome, Italy), pp. 3565–3572, IEEE, apr 2007.

[3] M. Bloesch, S. Omari, M. Hutter, and R. Siegwart, "Robust visual inertial odometry using a direct ekf-based approach," in *Intelligent Robots and Systems (IROS), 2015 IEEE/RSJ International Conference on*, pp. 298–304, IEEE, 2015.

[4] A. Barrau and S. Bonnabel, "An EKF-SLAM algorithm with consistency properties," tech. rep., 2016.

[5] C. Forster, M. Pizzoli, and D. Scaramuzza, "Svo: Fast semi-direct monocular visual odometry," in *IEEE International Conference on Robotics and Automation (ICRA)*, pp. 15–22, IEEE, 2014.

[6] R. Mur-Artal, J. M. M. Montiel, and J. D. Tardos, "ORB-SLAM: a versatile and accurate monocular SLAM system," *IEEE Transactions on Robotics*, vol. 31, no. 5, pp. 1147–1163, 2015.

[7] P. Lourenço, P. Batista, P. Oliveira, and C. Silvestre, "A globally exponentially stable filter for bearing-only simultaneous localization and mapping with monocular vision," *Robotics and Autonomous Systems*, vol. 100, pp. 61–77, feb 2018.

[8] S. Brás, R. Cunha, C. J. Silvestre, and P. J. Oliveira, "Nonlinear attitude observer based on range and inertial measurements," *IEEE Transactions on Control Systems Technology*, vol. 21, no. 5, pp. 1889–1897, 2013.

[9] T. Hamel and C. Samson, "Position estimation from direction or range measurements," *Automatica*, vol. 82, pp. 137–144, aug 2017.

[10] T. A. Johansen and E. Brekke, "Globally exponentially stable kalman filtering for SLAM with AHRS," in *Information Fusion (FUSION), 2016 19th International Conference on*, pp. 909–916, IEEE, 2016.

[11] E. Bjørne, T. A. Johansen, and E. F. Brekke, "Redesign and analysis of globally asymptotically stable bearing only slam," in *Information Fusion (Fusion), 2017 20th International Conference on*, pp. 1–8, IEEE, 2017.

[12] E. Bjørne, T. A. Johansen, and J. Delaune, "Estimating vector magnitude from its direction and derivative, with application to bearing-only slam filter problem," in *2018 IEEE Conference on Decision and Control (CDC)*, pp. 1353–1360, IEEE, 2018.

[13] D. Gálvez-López and J. D. Tardos, "Bags of binary words for fast place recognition in image sequences," *IEEE Transactions on Robotics*, vol. 28, no. 5, pp. 1188–1197, 2012.

[14] E. Bjørne, E. F. Brekke, and T. A. Johansen, "Cascade attitude observer for the slam filtering problem," in *Control Technology and Applications (CCTA), 2017 IEEE Conference on*, pp. 945–952, IEEE, 2017.

[15] H. F. Grip, T. I. Fossen, T. A. Johansen, and A. Saberi, "Attitude estimation using biased gyro and vector measurements with time-varying reference vectors," *IEEE Transactions on Automatic Control*, vol. 57, no. 5, pp. 1332–1338, 2012.

[16] E. Bjørne, *Globally Stable Observers for Simultaneous Localization and Mapping*. PhD thesis, Deptment of Engineering Cybernetics, Norwegian Univercity of science and Thecnology, Trondheim, 2019.

[17] T. Hamel and R. Mahony, "Attitude estimation on SO(3) based on direct inertial measurements," in *Proceedings 2006 IEEE International Conference on Robotics and Automation, 2006. ICRA 2006.*, pp. 2170–2175, IEEE, 2006.

[18] A. Morgan and K. Narendra, "On the stability of nonautonomous differential equations $dx/dt = [A + B(t)]x$, with skew symmetric matrix$B(t)$," *SIAM Journal on Control and Optimization*, vol. 15, no. 1, pp. 163–176, 1977.

[19] A. Loria and E. Panteley, "Uniform exponential stability of linear time-varying systems: revisited," *Systems & Control Letters*, vol. 47, no. 1, pp. 13–24, 2002.

[20] T. Fossen, A. Loría, and A. Teel, "A theorem for UGAS and ULES of (passive) nonautonomous systems: Robust control of mechanical systems and ships," *International Journal of Robust and Nonlinear Control*, vol. 11, no. 2, pp. 95–108, 2001.

[21] M. Jankovic and B. K. Ghosh, "Visually guided ranging from observations of points, lines and curves via an identifier based nonlinear observer," *Systems & Control Letters*, vol. 25, no. 1, pp. 63–73, 1995.

[22] F. Le Bras, T. Hamel, R. Mahony, and C. Samson, "Observers for position estimation using bearing and biased velocity information," in *Lecture Notes in Control and Information Sciences*, vol. 474, pp. 3–23, 2017.

[23] R. Spica and P. R. Giordano, "A framework for active estimation: Application to structure from motion," in *Proceedings of the IEEE Conference on Decision and Control*, pp. 7647–7653, 2013.

[24] S. Albrektsen and T. Johansen, "User-configurable timing and navigation for uavs," *Sensors*, vol. 18, no. 8, 2018.

[25] P. Furgale, J. Rehder, and R. Siegwart, "Unified temporal and spatial calibration for multi-sensor systems," in *Intelligent Robots and Systems (IROS), 2013 IEEE/RSJ International Conference on*, pp. 1280–1286, IEEE, 2013.

[26] P. Furgale, T. D. Barfoot, and G. Sibley, "Continuous-time batch estimation using temporal basis functions," in *IEEE International Conference on Robotics and Automation (ICRA)*, pp. 2088–2095, IEEE, 2012.

[27] V. Grabe, H. H. Bülthoff, D. Scaramuzza, and P. R. Giordano, "Nonlinear ego-motion estimation from optical flow for online control of a quadrotor UAV," *The International Journal of Robotics Research*, vol. 34, no. 8, pp. 1114–1135, 2015.

[28] J. Shi and C. Tomasi, "Good features to track," tech. rep., Cornell University, 1993.

[29] C. Tomasi and T. Kanade, "Detection and tracking of point features," 1991.

[30] A. Agarwal, C. Jawahar, and P. Narayanan, "A survey of planar homography estimation techniques," *Centre for Visual Information Technology, Tech. Rep. IIIT/TR/2005/12*, 2005.

[31] E. Malis and M. Vargas, *Deeper understanding of the homography decomposition for vision-based control*. PhD thesis, INRIA, 2007.

[32] P. Lourenço, B. J. Guerreiro, P. Batista, P. Oliveira, and C. Silvestre, "3-D inertial trajectory and map online estimation: Building on a GAS sensor-based SLAM filter," in *Control Conference (ECC), 2013 European*, pp. 4214–4219, IEEE, 2013.